Assessment by X-ray CT of the effects of geometry and build direction on defects in titanium ALM parts

Fabien Léonard[1], Samuel Tammas-Williams[1,2], Philip B. Prangnell[1], Iain Todd[2], Philip J. Withers[1]

[1]Henry Moseley X-ray Imaging Facility,
The University of Manchester, Grosvenor Street, Manchester M13 9PL, England,
fabien.leonard@manchester.ac.uk, samuel.tammas-williams@manchester.ac.uk,
philip.prangnell@manchester.ac.uk, philip.withers@manchester.ac.uk

[2]University of Sheffield, Department of Materials Science and Engineering, Sir Robert Hadfield Building, Mappin Street, Sheffield S1 3JD, England, i.todd@sheffield.ac.uk

Abstract
Additive layer manufacturing (ALM) has the potential to allow engineers almost complete freedom of design, with reduced material wastage and tooling costs, as well as shorter lead times on new designs. Unfortunately, most ALM processes invariably lead to porosity in the material deposited. The ALM process investigated here, selective electron beam melting (SEBM) of a powder bed, is no exception. Although it is known that defects do arise, with this process their dependence on the part geometry and the adopted build strategy has not been resolved. This is of key importance, because experiments have shown porosity can make an order of magnitude difference to the fatigue life of ALM components. X-ray computed tomography (CT) is an ideal tool for fully characterising in 3D the defects seen within ALM parts and has been applied here to study the effect of geometry and build direction on defects in titanium components. The most industrially, realistic worst case scenario was employed using an Arcam machine with a small raster pattern misalignment in order to study all the characteristic flow types possible in the SEBM process. For most of the test samples studied, XCT revealed large elongated pores (> 100 μm) to be present, which grew at a distance of around 1 mm from an edge, following the build direction. The position of this defect type correlated with the misaligned overlap region between the slow contour passes of the electron beam around the periphery of the sample outline and the hatching in fill region of a section. Smaller voids caused by gas entrapment were also resolved by XCT but they appeared to be mostly randomly distributed.

Keywords: CT, ALM, SEBM, 3D porosity measurements, 3D porosity distribution, Ti-6Al-4V, distance map.

1 Introduction

Additive layer manufacture (ALM) is a relatively new technique that could replace traditional, subtractive, manufacturing in many situations [1]. ALM works by dividing a CAD model into thin horizontal layers which are then built up on top of one another to create a 3D volume [1]. Complex shapes that could not previously be manufactured are possible allowing new and highly efficient designs which, combined with shorter lead times and reduced material and tooling costs, make this a very attractive proposition for a number of industries. Selective electron beam melting (SEBM) is one such ALM technique, which like many of the powder based methods [2-4] displays some level of porosity in the solid material (in our case titanium) produced [5,6]. These pores can be grouped based on their appearance and probable cause: roughly spherical gas pores, fusion defects caused by unmelted powder and defects in the build direction previously attributed to beam tripping [5]. Despite

the appearance of these pores, and the unusual microstructure associated with ALM, the static mechanical properties are good and comparable to wrought titanium [6-8]. The pores do however give rise to reduced life [3,4]. Scatter in the fatigue data of over an order of magnitude, in terms of the number of cycles to failure at the same stress level, has been observed in SEBM samples [6]. It has been found that pores near the edge of test specimens cause the most dramatic reduction in fatigue life, while those at the centre are less detrimental [6]. Since it is necessary to design for the lowest value, this leads to a very inefficient use of material. It is thus crucial to understand how likely pores are to appear, and how they are distributed within components as a function of part geometry and the processing conditions. In order to get a "warts and all", worst case scenario of the porosity, non-optimum beam alignment settings were used here. This is likely to be the worst case that may be found in an industrial setting.

2 Experimental

2.1 Specimens

Three standard shapes, prismatic, cubic and cylindrical, were chosen to represent possible geometry elements in engineering components, as shown in Figure 1. All samples had the same maximum dimension (15 mm) ensuring similar spatial resolution under X-ray CT. Two to three different build orientations were used for each of the geometries. The parts were produced using an Arcam S12 EBM machine, based in the University of Sheffield, with pre-alloyed Ti-6Al-4V powder. Standard melt settings, according to the EBM Control 3.2, Service Pack 1 software for a layer thickness of 70 µm, but with a small error between the alignment of the contour pass and the hatching patterns were used. In each deposition cycle, the beam is first used to preheat and sinter the powder, this is followed by a contour pass of the outer edges of each section, using a slow highly focused and then in-fill hatching with a faster, less focused, but more powerful beam. It should be noted the hatching direction alternates by 90° every other layer.

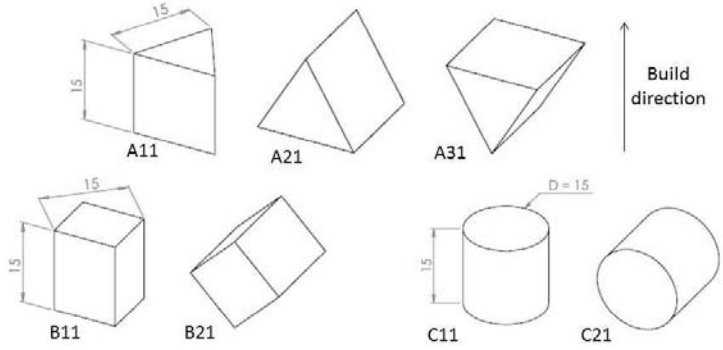

Figure 1: Geometries of specimens under investigation, A prism, B cube, and C cylindre (dimensions are in mm).

2.2 X-ray CT

The ALM specimens were scanned at the Henry Moseley X-ray Imaging Facility in Manchester on a Nikon Metrology 225/320 kV Custom Bay machine. The system was equipped with a 225 kV static multi-metal anode source (Cu, Mo, Ag, and W) with a minimum focal spot size of 3 µm and a Perkin Elmer 2000 × 2000 pixels 16-bit amorphous silicon flat panel detector.

Scanning was performed with a silver target using a voltage of 160 kV and a current of 110 µA, using Nikon Metrology proprietary acquisition software (InspectX version XT 2.2 service pack 5.5). The data acquisition was carried out with an exposure time of 1415 ms and a 1.5 mm copper filter to avoid

saturation of the detector. The number of projections was set to 3142 and the number of frames per projection was 1, resulting in an acquisition time of 1 hour and 15 minutes. The correction images were acquired by averaging 128 frames using the exact X-ray conditions as used for the acquisition.

Reconstruction was performed with Nikon Metrology proprietary software CT-Pro. The beam hardening correction setting was set to 1 (out of a range of 1–6) whereas the noise reduction setting was set to 2 (out of a range of 1–6) and interpolation was used. The entire volume (2000 × 2000 × 2000 voxels) was reconstructed at full resolution with a voxel size of 9.9 µm along the *x*, *y*, and *z* directions. In order to visualise and process the data, the data set had to be reduced. The data were loaded into Volume Graphics proprietary software VGStudio MAX® and then converted from 32 bits to 8 bits with the grey scale remapped from [0,150] to [0,255].

The visualisation software employed was Visualization Sciences Group proprietary software Avizo® Fire version 7.0.1. The segmentation strategy adopted was to first segment the outside of the specimen using the magic want tool for grey values in the range [0,100]. The selection was then inverted and applied to a material labelled "*ALM*". Within the *ALM* selection, a threshold was applied to segment the porosity with an interval of [0,100], and the selection was then applied to a material labelled "*Voids*".

A new approach to characterising the 3D porosity distribution was used based on the *void-to-edge distance* which can be obtained from Avizo® by combining the distance map of the ALM part with the segmented voids, as shown in Figure 2. As a result, the distance of every voxel segmented as voids to the closest edge can be measured over the entire 3D volume.

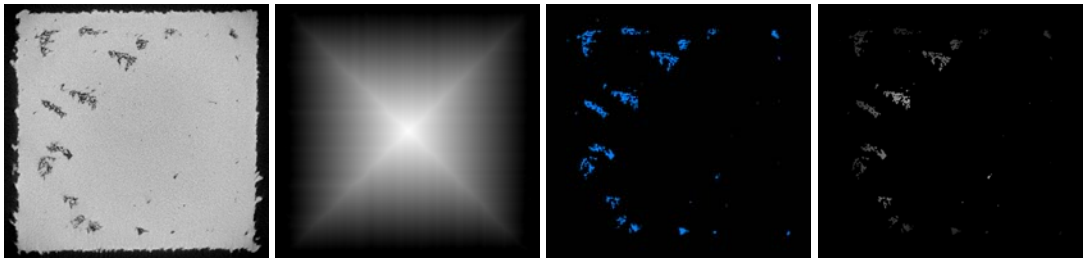

a) raw 2D slice b) ALM distance map c) segmented voids d) void-to-edge distance map

Figure 2: Workflow path to obtain the void-to-edge distance measurements (9.54 × 9.16 mm images).

3 Results

X-ray computed tomography allows a full non-destructive characterisation of the porosity contained within the ALM specimens. As will be discussed further below, some specific samples were found to contain large 'wormhole' defects near their edge caused by the contour and hatching pattern misalignment error; whereas all samples contained a similar distribution of fine gas pores. The quantification performed on the voids is summarised in Table 1. For all specimens the minimum equivalent void diameter[2] detected was around 0.020-0.035 mm. Smaller pores than this have in fact be seen by microscopy in ALM parts, down to a size of 10 µm and this threshold is therefore

[2] The equivalent diameter is the diameter the void would have if it was perfectly spherical.

determined by the resolution of the tomography measurement which is around 20 µm. The range of the maximum equivalent diameter varied significantly between samples; namely between 0.25 mm and 1.7 mm. However, values of mean equivalent diameter were relatively consistent between the different specimens ranging from 0.05 to 0.07 mm, because the far higher number of small gas pores dominated the statistics. As a result, the standard deviation values were also similar. The pore volume fractions varied between specimens, but remained well below 1 %.

Table 1: Summary of porosity equivalent diameter measurements.

Specimen label	Minimum mm	Maximum mm	Mean mm	Standard deviation mm	Volume fraction %
A11	0.033	1.173	0.063	0.044	0.221
A21	0.021	0.263	0.051	0.024	0.016
A31	0.036	0.571	0.069	0.041	0.063
B11	0.022	1.196	0.056	0.073	0.291
B21	0.021	1.732	0.050	0.064	0.538
C11	0.032	0.233	0.062	0.019	0.009
C21	0.021	0.943	0.049	0.048	0.114

3.1 Triangular prisms (A specimens)

The triangular geometry samples were made using three different build directions, the corresponding segmented volumes are presented in Figure 3. Small pores can be observed in all three specimens, but relatively large “wormhole” pores were only seen in specimens A11 and A31. In specimen A11, these large pores were located close to the sample edges and propagated along the edge following the build direction (vertically), whereas in specimen A31, larger pores were also located close to the bottom edge lying perpendicular to the build direction.

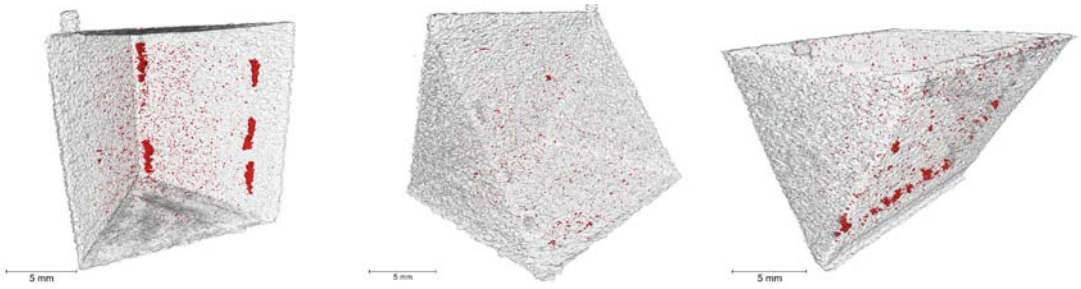

a) A11 b) A21 c) A31

Figure 3: 3D rendering of triangular ALM specimens (voids are shown in red, build direction is vertical).

Figure 4 summarises the void equivalent diameter distributions and the void-to-edge distance distributions seen for the triangular geometry samples. From the equivalent diameter distributions, no clear differences can be seen between the build directions for the main distribution peaks, which are dominated by the high density of small gas pores. However, the distributions had different length tails which reflects the different tendencies for a small number of large defects to be seen within each build. In all cases, the frequency distributions were dominated by gas pores and the number of pores with an equivalent diameter above 100 µm was negligible. The void-to-edge distance graph shows a peak around 1 mm for all specimens, which indicates that for all three configurations there is a much greater probability of finding voids at a distance of 1 mm from a section edge. Specimen A21 gave slightly different results with a stronger peak at a distance of 0.07 mm from the edge, which corresponds to the

concentration of small porosity seen located very close to the base plane of this specimen. However the peak around 1 mm, from the section walls, although weaker than for specimens A11 and A31, is still present.

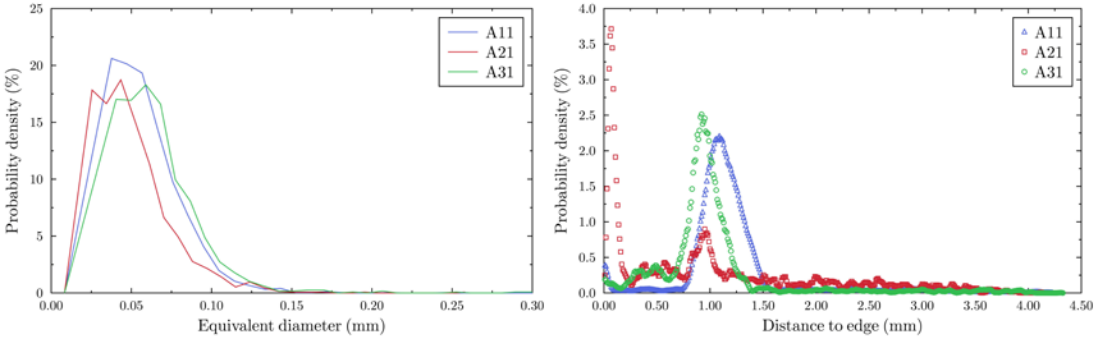

a) equivalent diameter distribution b) void-to-edge distance distribution

Figure 4: Statistical distribution of defects in the triangular prisms.

3.2 Cubic samples (B specimens)

The cubic samples were built using two build directions and the corresponding segmented volumes are presented in Figure 5. Small gas pores and large worm hole pores could be observed in both specimens, but their positioning was different. In specimen B11, the large pores were located in a similar way to those in specimen A11: close to the edges and propagating along the edge following the build direction (vertically). In comparison, specimen B21 had features similar to specimen A21 with large pores located close to the bottom edge, but lying perpendicular to the build direction. A large density of pores was also evident, located on a plane parallel to the back face.

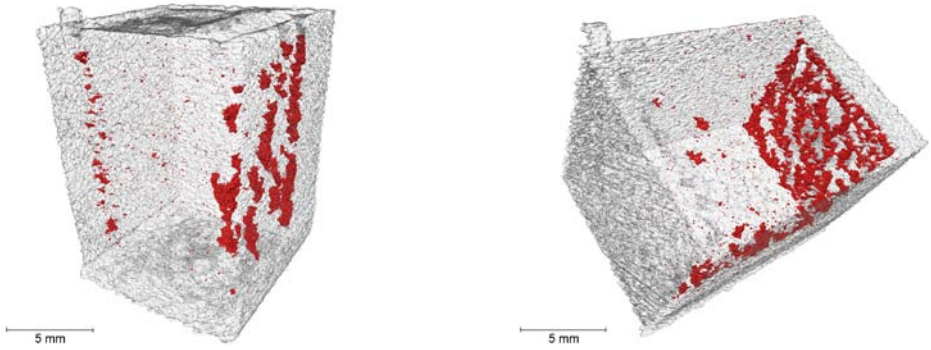

a) B11 b) B21

Figure 5: 3D rendering of the ALM cubic sample (voids are shown in red, build direction is vertical).

Again there were no clear differences between the main peaks in the equivalent diameter distributions for similar reasons to those discussed above (Figure 6a) and the number of pores with an equivalent diameter above 100 µm was very small. The void-to-edge distance graph confirmed the consistent presence of a sharp peak around 1 mm from the specimen edge for sample A11. Specimen A21 also had a peak at a value just below 1 mm, but the number density was much lower, with an increased density for defects to be present at distances above 1 mm. However, in this case the distribution was skewed due to the presence of a higher pore density on the plane parallel to the back face.

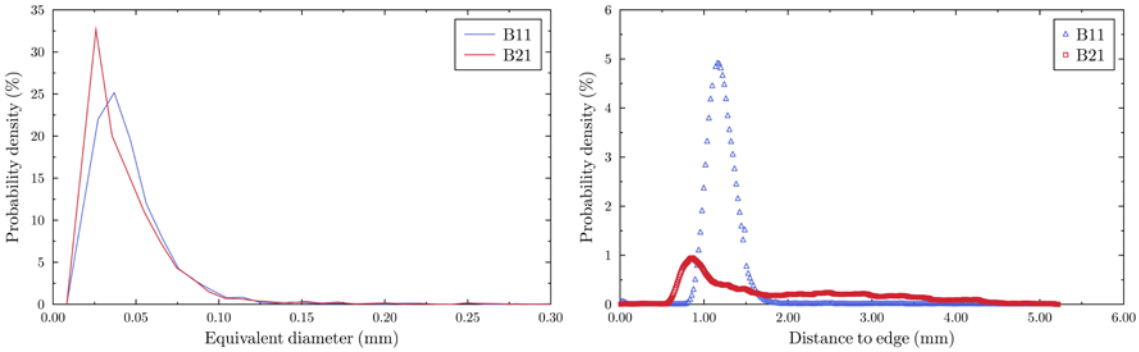

a) equivalent diameter distribution b) void-to-edge distance distribution

Figure 6: Statistical distributions of defects in the cubic specimens.

3.3 Cylindrical samples (C specimens)

Two circular parts were built using different build directions and the corresponding segmented volumes are presented in Figure 7. For specimen C11, it appears that only small voids were present and these were relatively randomly distributed over the specimen volume. On the other hand, specimen C21 also had larger wormhole-like pores which followed the build direction and the curvature of the cylindrical surface.

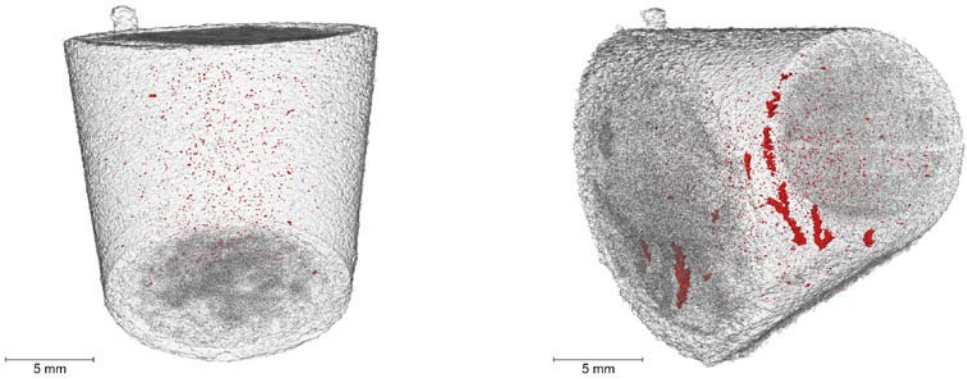

a) C11 b) C21

Figure 7: 3D rendering of ALM cylindrical specimens (voids are shown in red, build direction is vertical).

In Figure 8a, it can be noted that as a result of the absence of large scale defects the maximum of the equivalent diameter distribution was at a lower diameter for specimen C21 than for specimen C11. The void-to-edge distance graph showed a sharp peak around 1 mm for specimen C21, whereas no peak could be observed for specimen C11. This absence of peak demonstrates that the porosity distribution was more uniform within the volume of specimen C11.

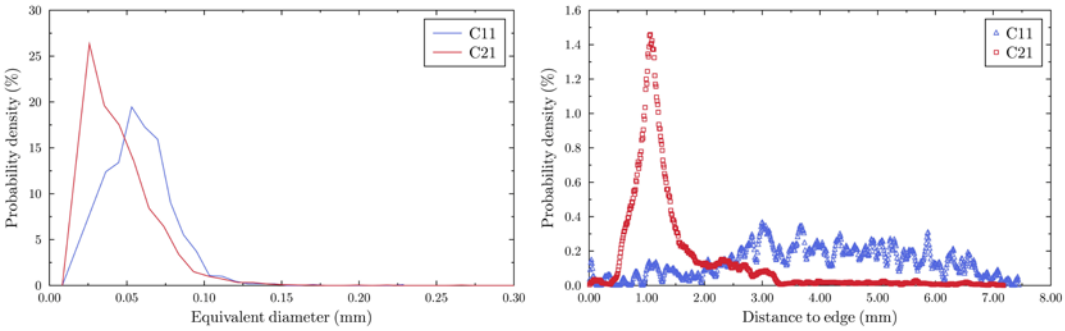

a) equivalent diameter distributions b) void-to-edge distance distributions

Figure 8: Statistical distribution of defects in the cylindrical specimens.

4 Discussion

Quantification of the void equivalent diameters measured for defects in ALM parts from tomographic data has demonstrated that, while the equivalent diameter distributions do not vary significantly from one specimen to another, a large variation in the pore diameters was evident for all the samples when there is a misalignment error in the build parameters. Consequently, neither the mean diameter value, nor the equivalent diameter distribution are appropriate measures of characterising the pore distributions from a fatigue lifing viewpoint, for which the size and location of the largest pores within the volume will be much more important. This is because pore size number distributions were dominated by the large number of very small gas pores found in the ALM builds, which were not greatly affected by geometry. In contrast, the much larger defects detected (which will have a greater impact on fatigue crack initiation if careful quality control is not followed) varied greatly in density and position between samples, being affected both by the component geometry and build position. In this context, it is therefore essential to employ a method that reveals more statistical information about the large pores in a tomography data set. One such approach is the Feret shape versus the equivalent diameter plot, as shown in Figure 9. This plot emphasises the number of large pores, but also provides information about their shape. For example in Figure 9a, it is possible to distinguish between the large elongated voids from specimen A11 (Feret shape value above 2) and the large more spherical voids (Feret shape value below 2) located close to the bottom edge of the specimen A31.

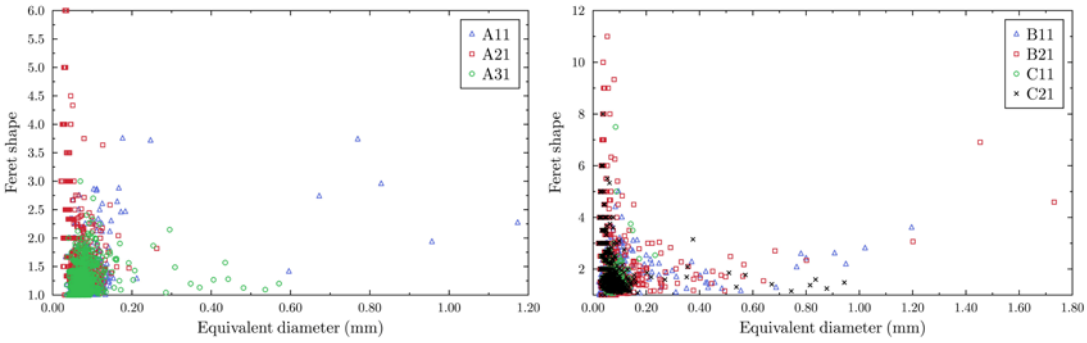

a) triangular prisms c) cubic and cylindrical specimens

Figure 9: Feret shape versus equivalent diameter.

Except for specimen C11, all specimens exhibited a peak in porosity at around 1 mm in the void-to-edge distance distribution plot. For specimen C11, the porosity distribution in the specimen was more uniform and is consistent with the absence of large voids. When large voids were present, they tended to grow at a distance of 1 mm from a section edge, following the build direction. Such voids grow up through many deposited layers and thus have the appearance of tunnel defects or 'wormholes'. Figure 10 clearly illustrates this effect, which persisted even when oblique or circular edges are present. The distance of 1 mm from the section edge, where such defects were found to be located, correlates with the width of the three initial contour passes of the electron beam, which draws the outline of each section in the powder bed. The first is offset 0.3 mm from the section edge followed by two further passes each offset 0.25 mm from the previous. Taking into account the size of a melt pool of 0.6 mm, this would give an initial solidified outline pass of $\geq$ 1.05 mm. Thus, tomography has shown that such defects appear to develop between the overlap of the contour and infill hatching raster patterns when there is a small alignment error between them. Similar large voids have been previously observed in the literature [5] where they were attributed to beam tripping. Here tomography has shown that they can be more extensive than previously thought and stem from a poor alignment set-up in the EBSM machine.

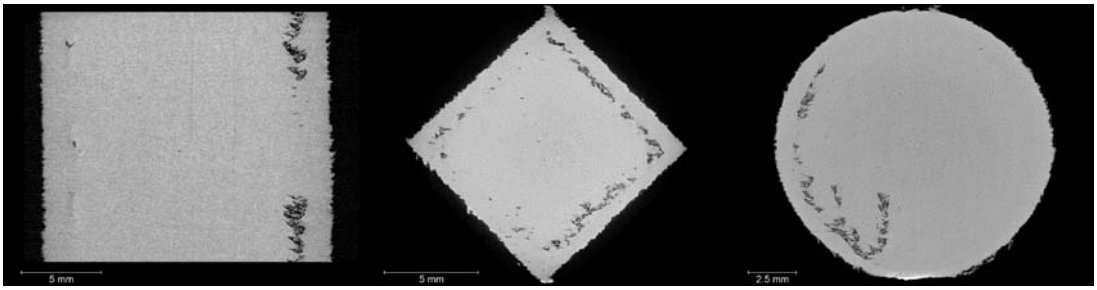

a) A11 b) B21 c) C21

Figure 10: Example of large porosity following the build direction (build direction is vertical).

5 Conclusion

It has been demonstrated that X-ray computed tomography is a powerful tool for fully characterising, in 3D, the typical defects seen in titanium ALM components. Not only can the whole specimen be examined, but the exact size, shape, maximum dimension and location of the pores can be obtained whilst it is impossible from 2D metallographic sections. Furthermore, XCT can locate critical defects that could easily be missed in single metallographic sections, as well as general porosity. Such information is extremely useful for further understanding the ALM manufacturing process and the tolerances to errors in the equipment calibration procedures. Overall, the void-to-edge distance approach is believed to be an innovative way of extracting quantitative 3D information about the spatial distribution of voids within ALM structures, whereas the Feret shape plot is a better method to characterise the dimensions of large defects.

Acknowledgements

The authors acknowledge funding from EPSRC for the Henry Moseley X-ray Imaging Facility under EP/F007906/1 and EP/F028431/1 grants and from the Advanced Metallic Systems CDT at the Universities of Manchester and Sheffield.

References

[1] Gibson I, Rosen DW, Stucker B. Additive Manufacturing Technologies. London: Springer, 2010.

[2] Thijs L, Verhaeghe F, Craeghs T, Humbeeck JV, Kruth J-P. Acta materialia 2010;58:3303-3312.

[3] Amsterdam E, Kool G. Icaf 2009, bridging the gap between theory and operational practice 2009:1261–1274.

[4] Santos EC, Osakada K, Shiomi M, Kitamura Y, Abe F. Proceedings of the institution of mechanical engineers, part c: journal of mechanical engineering science 2004;218:711-719.

[5] Gaytan SM, Murr LE, Medina F, Martinez E, Lopez MI, Wicker RB. Materials technology 2009;24.

[6] Antonsamy AA. Microstructure, Texture and Mechanical Property Evolution During Additive Manufacture of Ti6Al4V Alloy Using Laser, Electron Beam, and Arc Melting Techniques for Aerospace Applications. University of Manchester, 2012.

[7] Al-Bermani SS, Blackmore ML, Zhang W, Todd I. Metallurgical and materials transactions a 2010;41:3422-3434.

[8] Brandl E, Leyens C, Palm F, Onteniente P. Wire instead of powder properties of additive manufactured ti-6al-4v for aerospace applications. In: Euro-uRapid. Berlin: 2008.